Available online at www.sciencedirect.com
ScienceDirect
Energy Reports 9 (2023) 149–161
www.elsevier.com/locate/egyr

TMREES23-Fr, EURACA 06–08 February 2023, Metz-Grand Est, France

Evaluation of high-tensile steel using nonlinear analysis: Experiment-FE materials benchmarking of LNG carrier structures under low-temperature conditions

Suryanto Suryanto[a], Aditya Rio Prabowo[a,*], Teguh Muttaqie[b,*], Iwan Istanto[c], Ristiyanto Adiputra[b], Nurul Muhayat[a], Aprianur Fajri[a], Moritz Braun[d], Sören Ehlers[d,e]

[a] *Department of Mechanical Engineering, Universitas Sebelas Maret, Surakarta 57126, Indonesia*
[b] *Research Center for Hydrodynamics Technology, National Research and Innovation Agency (BRIN), Surabaya 60117, Indonesia*
[c] *Department of Electro-Mechanical, Polytechnic Institute of Nuclear Technology, Yogyakarta 55281, Indonesia*
[d] *Institute of Maritime Energy Systems, German Aerospace Centre (DLR), Geesthacht 21502, Germany*
[e] *Institute for Ship Structural Design and Analysis, Hamburg University of Technology, Hamburg 21073, Germany*

Received 16 May 2023; accepted 28 May 2023
Available online xxxx

Abstract

Natural gas is the cleanest energy source compared to other fossil fuels. When the temperature is between −160 ºC to −164 ºC at atmospheric pressure, natural gas will be in liquid form, commonly called Liquefied Natural Gas (LNG). Currently, the demand for the availability of natural gas is increasing rapidly. However, not all countries have natural gas reserves. In this case, ships transport Liquefied Natural Gas (LNG) between continents and oceans to meet global needs. Since the Northern Sea Route (NSR) was opened, the route has become an alternative route where ships can save fuel because the distance is closer than the standard route (through the Suez Canal). However, because this route is in the Arctic region, which has a harsh environment, the ship may experience a structural failure, resulting in an accident and possibly causing material, human or other casualties. This paper employed the finite element method to observe the materials used as raw materials for the structure of natural gas shipping vessels. High tensile steel grade AH 32 was tested for tensile using numerical analysis. The temperature varied from room to shallow temperature (−160 ºC). Besides that, the mesh sizes used were 1 mm, 2 mm, 4 mm, 6 mm, 8 mm, and 10 mm to produce outcomes that are most similar to earlier research assessed via experimental testing. The result obtained was that the mechanical properties of AH 32 steel will change significantly at shallow temperatures, which can be observed from the engineering stress–strain graph. High tensile steel grade AH 32 becomes very brittle at −160 ºC. Besides that, the necking phenomenon, as in the experimental test, can also be observed through numerical analysis.

Peer-review under responsibility of the scientific committee of the TMREES23-Fr, EURACA, 2023.

Keywords: Natural gas; Liquefied natural gas; Tensile test; Numerical analysis; Necking phenomenon

* Corresponding authors.
E-mail addresses: aditya@ft.uns.ac.id (A.R. Prabowo), teguh.muttaqie@brin.go.id (T. Muttaqie).

https://doi.org/10.1016/j.egyr.2023.05.252

Peer-review under responsibility of the scientific committee of the TMREES23-Fr, EURACA, 2023.

1. Introduction

Natural gas is one of the most preferred energy resources due to lower greenhouse gas emissions than non-renewable energy resources [1]. In contrast to oil and coal, natural gas is the cleanest fossil energy with high efficiency, nearly zero nitrogen and sulfur compounds emission, and low carbon dioxide emissions [2,3]. Natural gas will be in a liquid state when the temperature range is −160 °C to −164 °C (at atmospheric pressure). In the liquid phase, natural gas is better known as Liquefied Natural Gas (LNG). Liquefied Natural Gas (LNG) is a type of energy with a high heat value and suitable energy and is relatively inexpensive [4]. Liquefied Natural Gas consists primarily of methane [5,6], a simple compound having a carbon atom surrounded by four hydrogen atoms. Methane is highly flammable and burns almost completely [7]. For several decades, Liquefied Natural Gas has grown in global consumption due to its wide applications in various fields, such as the industrial sector, power generation, and shipping alternative fuel [8–10]. However, based on the chemical compositions, LNG may cause fire and explosion, so loading/unloading, bunkering, storage, and transportation of LNG fuel is an operation that requires great attention.

The demand for natural gas is increasing every year, so world trade is also increasing [11]. For trading activities to continue, there needs to be a liaison between suppliers and users. Primarily, natural gas is supplied to world markets in two ways, by pipelines and the carrier. In less than 1000 km, pipelines are more feasible and economical than carriers. However, the pipeline is considered too risky if it is longer than 3500 km, whereas the carrier is technically more feasible [12]. Natural gas shipped by ship is usually in liquid form (i.e., LNG). There are several choices of world natural gas trade routes, such as the Northwest Passage (NWP), the Northeast Passage (NEP), and the traditional Europe–Asia route (the Suez Canal Route (SCR)) [13,14]. The Northeast Passage (NEP) is a maritime route that connects the Atlantic Ocean with the Pacific Ocean through the northern coastline of Russia [15]. The part of the NEP between the Bering Strait and Novaya Zemlya is called the North Sea Route (NSR) [10,16]. When sea ice and ice thickness decrease rapidly due to global warming, it opens up opportunities for traders to pass the NSR. However, ships passing through the North Sea Route must be equipped with icebreakers for safety and security [17]. Compared to the traditional sea route (the Suez Canal Route), NSR brings Europe to Asia closer [18,19], which reduces fuel, time, costs, and emissions during shipping [20–22]. Since 2017, this route has increased by 194.5% [23]. In 2016–2019 cargo traffic experienced a rapid increase, from 7.5 million tons to 31.5 million tons (a 4-fold increase) [24].

However, considering the NSR is in the Arctic region, several risks and challenges must be faced. Unpredictable weather conditions, shallow temperatures, lack of communication and navigation aids, and remoteness are risks that may occur in this region [13]. Shallow temperature conditions can impact the ship's structure. The material composition of the structure creates an issue, being more brittle or ductile. Nam and Amdahl [25] conducted brittle fractures in ships and offshore structures in the arctic region. On the other hand, previous studies researched the resistance of structures to arctic conditions using numerical methods [26,27]. They concluded that the structural resistance depends on material properties from the uniaxial tensile tests. Material characterization, such as yield stress, ultimate stress, and failure strain, change significantly when the temperature is lower. Thus, it is necessary to pay special attention when selecting ship materials adapted to the use and terrain the ship will take.

This paper discusses the response of materials used in ship structures to shallow temperatures using numerical methods. Previous studies have experimentally carried out material responses to low temperatures, which will be used to evaluate this study [28]. This research is structured as follows. The experimental procedures carried out by previous researchers and the numerical configurations used in this study are described in Section 2. Section 3 presents the results and discussion of this study. Mesh convergence is used to get a variety of results. The mesh sizes used were 1 mm, 2 mm, 4 mm, 6 mm, 8 mm, and 10 mm. Finally, Section 4 concludes and makes suggestions for further research.

2. Methodology

2.1. Laboratory experiment set-up

Experiments conducted by Paik et al. (2020) to observe the tensile test using high tensile steel grade AH 32 with temperature variations used ranging from 20 °C (room temperature), −40 °C, −80 °C, −100 °C, −130 °C and −160 °C. Table 1 presents the mechanical properties of AH 32 steel at room temperature. At low temperatures,

the tensile test specimen used complies with ASTM E8/E8M (2015) as shown in Fig. 1. In the grip section of the tensile test specimen, holes were given so that it did not come off easily when installed on the universal testing machine. To reduce the temperature of the specimen until it reached the desired temperature, the specimen is given Liquefied Nitrogen Gases (LNG) with a cooling rate of −5 °C/min for 30 min [29]. The universal testing machine was equipped with a chamber to keep the temperature from changing when testing was carried out, as shown in Fig. 2a.

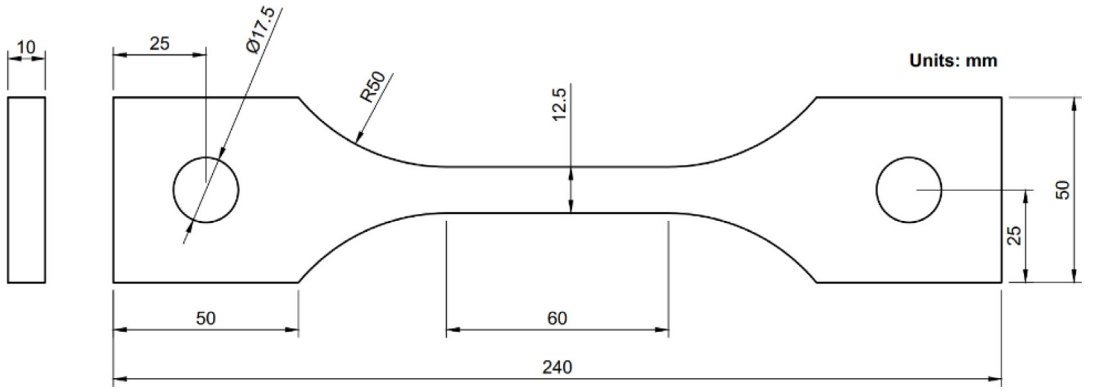

Fig. 1. Dimensional drawings of tensile test specimen.

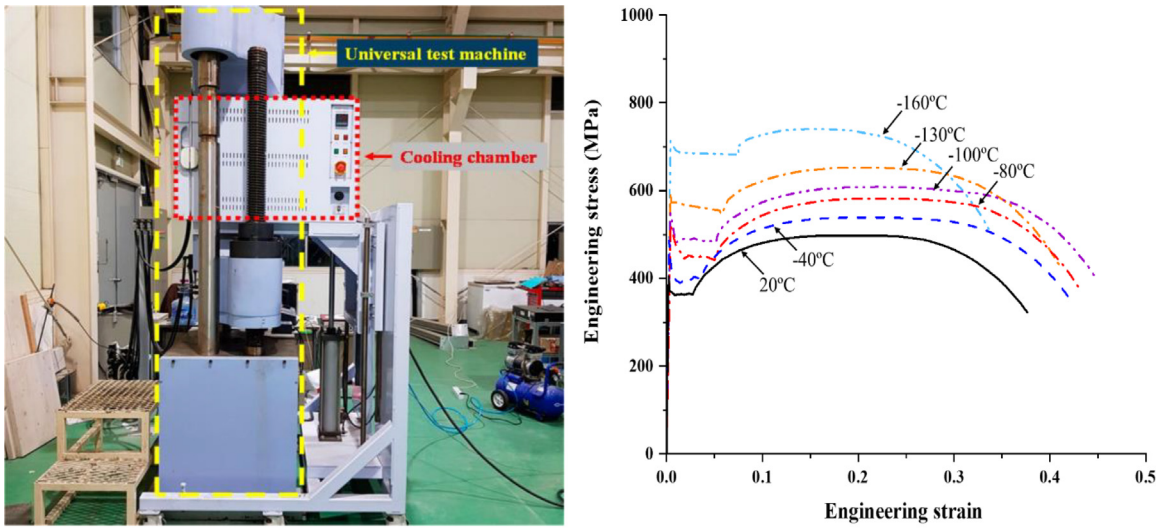

(a) (b)

Fig. 2. Experiment set-up and result [28]: (a) universal testing machine with cooling chamber and (b) engineering stress–strain curve.

After experiments, the results are shown in Fig. 2b. The experimental results showed that the lower temperature of the specimen, the higher the yield strength, ultimate strength, and fracture strain of the specimen. In addition, the elastic modulus obtained did not change even when subjected to different temperature treatments. From the experimental results, when the specimen temperature was lower than −100 °C, the yield strength, ultimate strength, and fracture strain would decrease.

Table 1. Mechanical properties of AH 32 steel at 20 ℃ (room temperature) [28].

Modulus Young (GPa)	Yield strength (MPa)	Ultimate tensile strength (MPa)	Ultimate fracture strain (-)	Fracture strain (-)
205.8	358.03	497.07	0.193	0.376

2.2. Numerical configuration

This study used ANSYS Explicit Dynamic code for non-linear numerical analysis [30–37]. The algorithm used in this code is presented as follows (Eqs. (1) and (2))

$$\{a_t\} = [M]^{-1}\left(\{F_t^{ext}\} - \{F_t^{int}\}\right) \tag{1}$$

$$F^{int} = \sum\left(\int_{\Omega}\left(B^T\sigma_n d\Omega + F^{hg}\right) + F^{cont}\right) \tag{2}$$

where $\{a_t\}$ is the acceleration at time t, $[M]$ is the mass matrix, F_t^{ext} is the external force vector, and F_t^{int}. F^{hg} is the hourglass resistance force, B^T is the form identical to the linear discrete strain–displacement matrix, F^{cont} is the contact force, Ω is the solid volume, and σ_n is the internal stress. In this algorithm, velocity and displacement are obtained through the following Eqs. (3)–(5)

$$\left\{v_{t+\Delta t/2}\right\} = \left\{v_{t-\Delta t/2}\right\} + \{a_t\}\,\Delta t_t \tag{3}$$

$$\{u_{t+\Delta t}\} = \{u_t\} + \left\{v_{t+\Delta t/2}\right\}\Delta t_{t+\Delta t/2} \tag{4}$$

$$\{x_{t+\Delta t}\} = \{x_0\} + \{u_{t+\Delta t}\} \tag{5}$$

where $\{v_t\}$ is the velocity at time t, $\{u_t\}$ is the displacement at time t, $\{x_0\}$ is the initial geometry, $\{x_0\}$ is the updated geometry at time t, $\{x_t\}$ is the difference in time at time t compared the initial condition.

The boundary conditions used in this study are shown in Fig. 3. By adjusting the opposite axial nodal force acting on both sides of the specimen until fracture [38,39]. The axial nodal force was selected using the volume box. Script "A" shows the side of the specimen that will move to the minus x-axis (right) and script "B" shows the side of the specimen that will move to the plus x-axis (left). The meshing process was performed by the automatic method. In addition, the mesh size was determined by setting the element size. To obtain varying results, the mesh sizes used were 1 mm, 2 mm, 4 mm, 6 mm, 8 mm, and 10 mm. The simulation was done until the test object broke, namely the end time was 1×10^{-4} s. This condition limit was applied to all variations that had been determined. The resulting data output in the form of equivalent plastic strain and normal stress were plotted on the x-axis and y-axis, respectively.

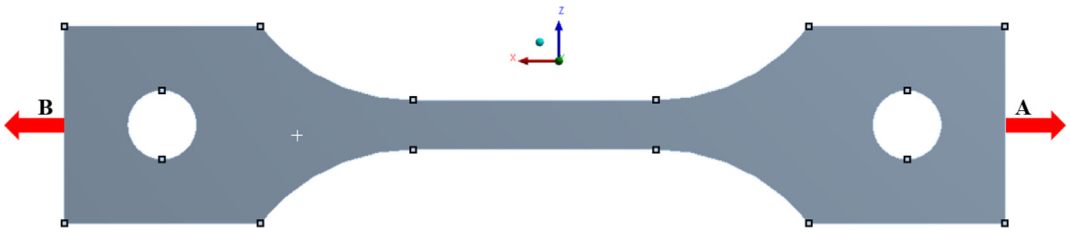

Fig. 3. Boundary conditions of tensile test with ANSYS Explicit Dynamic code.

Furthermore, setting the material model in Ansys software can be done on data engineering. The setting of the material model in this study is briefly presented in Fig. 4. It began by using the engineering stress–strain curve from previous research. Then determined the elastic–plastic parameters such as Young's modulus, yield stress, ultimate strength, and others. Then converted the engineering stress–strain curve into a true stress–strain curve. After that, put it into the plasticity table (multilinear isotropic hardening), and repeated it at all predetermined temperatures.

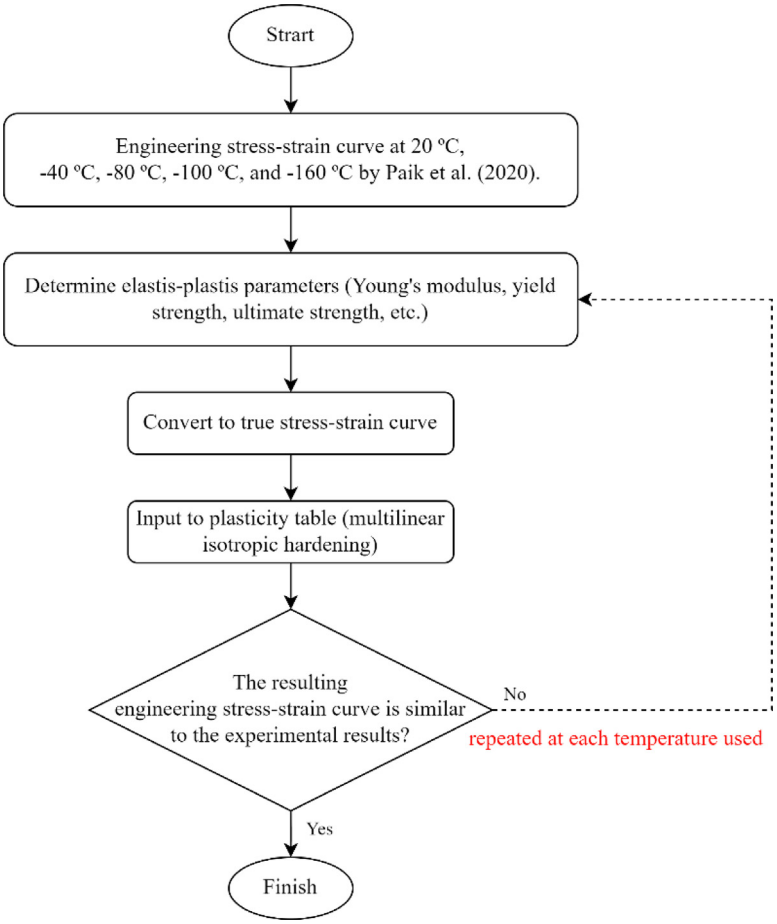

Fig. 4. Flowchart for setting the material model.

3. Results and discussion

The results from the current simulation showed similarities to the previous experimental results. Process the specimen during the simulation until a fracture occurred and produced a stress–strain curve, shown in Fig. 5. The resulting curve can be divided into two parts: linear and non-linear. The slope of the stress and strain curves characterized a linear section, otherwise it was a non-linear section. Young's modulus was determined in the linear section, by dividing the stress by the strain. The boundary between the linear and non-linear sections was the yield strength. At the start of the non-linear section, the stress increased with the strain. This phenomenon is called strain hardening because the resistance of steel is directly proportional to the increase in strain [40]. Then there was a slight increase in load, causing a significant increase in strain. If assumed that the volume is constant, the increase in strain will cause a reduction in the cross-section. This phenomenon is called necking. The stress at which the maximum load is reached is called tensile strength. After that, the engineering stress–strain curve decreases until failure occurred.

The engineering stress–strain curve was derived from the local stress–strain curve, which was determined segment by segment. The first segment assumed a yield stress slope, simulations in ANSYS were performed, and the resulting elongation and forces were compared to the measured values. Based on this comparison, the slope of the curve was iteratively changed until the force and elongation matched the values measured within the tolerances. The same was done in the second and subsequent segments until the specified iteration, as illustrated in Fig. 6. Afterwards, the local stress–strain curve can be converted into an engineering stress–strain curve

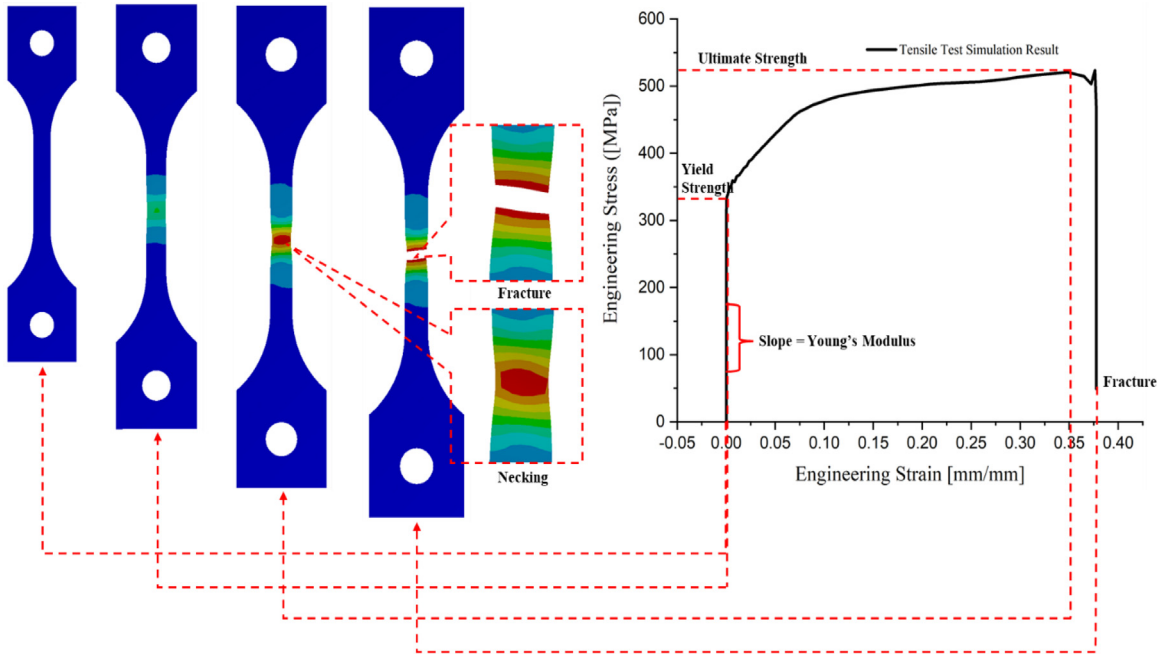

Fig. 5. Stages of the specimen during the simulation.

The engineering stress (σ) was calculated by the force acting (F) with respect to the cross-sectional area of the gauge length (A). The mathematical form of the description is presented in Eq. (6).

$$\sigma = \frac{F}{A} \tag{6}$$

The engineering strain (ε) was calculated with the elongation of the gauge length (Δl) respect to the initial gauge length (l_0). The mathematical form of the description is presented in Eq. (7).

$$\varepsilon = \frac{\Delta l}{l_0} \tag{7}$$

When the simulation was compared to the experimental results, great similarity in the engineering stress–strain curves was observed, as shown in Fig. 7. Nevertheless, the ultimate strength and fracture strain determined from the current simulation seem to be comparable. For more details, the data is presented in Table 2.

Table 2. Comparison of ultimate strength and fracture strain with laboratory experiment by Paik et al. [28].

Temperature (°C)	Ultimate strength (MPa)			Fracture strain (-)		
	Laboratory experiment	Current simulation	Errors (%)	Laboratory experiment	Current simulation	Errors (%)
20	497.07	520.56	4.73	0.336	0.37761	12.38
−40	537.81	553.99	3.00	0.409	0.42195	3.166
−80	579.13	626.3	8.15	0.448	0.43116	3.75
−100	605.10	648.12	7.11	0.430	0.44941	4.51
−130	652.28	675.42	3.54	0.423	0.4064	3.92
−160	739.36	779.07	5.37	0.376	0.34003	9.56

Apart from ultimate strength and fracture strain, other mechanical properties can also be determined through tensile tests. Toughness and ductility are two crucial mechanical properties. Toughness is the ability of a material to absorb energy and undergo plastic deformation before fracture. At the same time, ductility is measured by the degree of plastic deformation maintained at fracture. Then, ductility can be expressed quantitatively through the

Curve segment	Iteration	The process of determining the local stress-strain curve
1	1	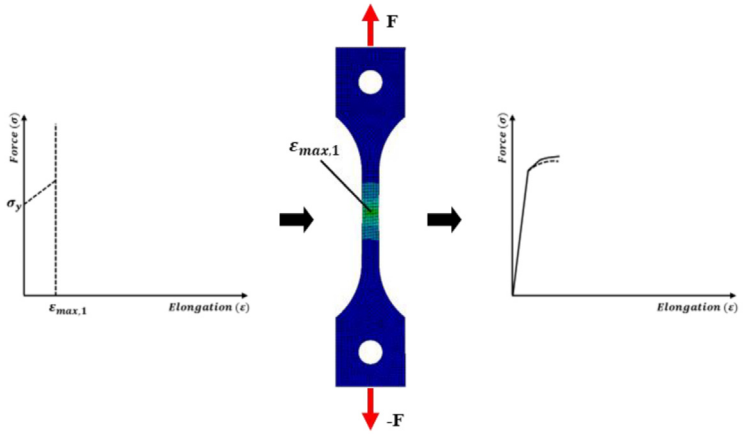
1	2 … n	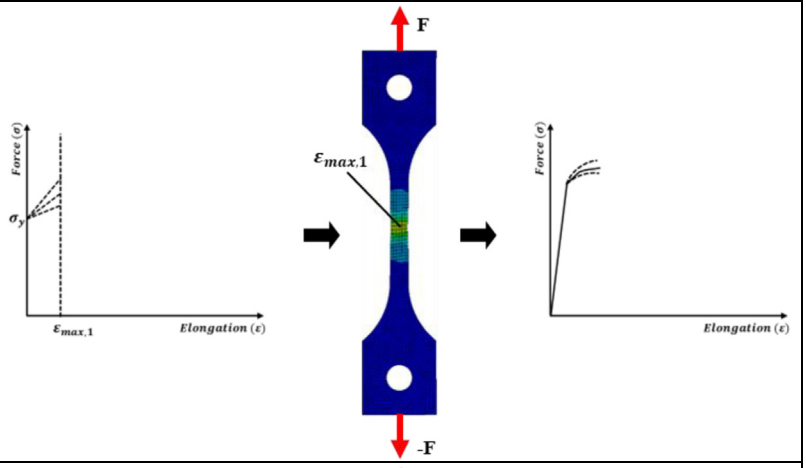
2	1	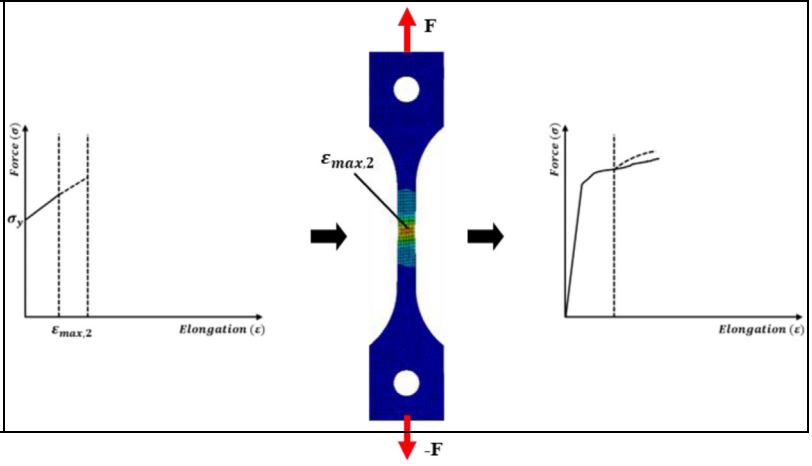

Fig. 6. Segment by segment to determine local stress–strain curve.

percentage of elongation (Eq. (8)) or the percentage reduction in the area of Eq. (9).

$$\%EL = \left(\frac{l_f - l_0}{l_0}\right) \times 100 \tag{8}$$

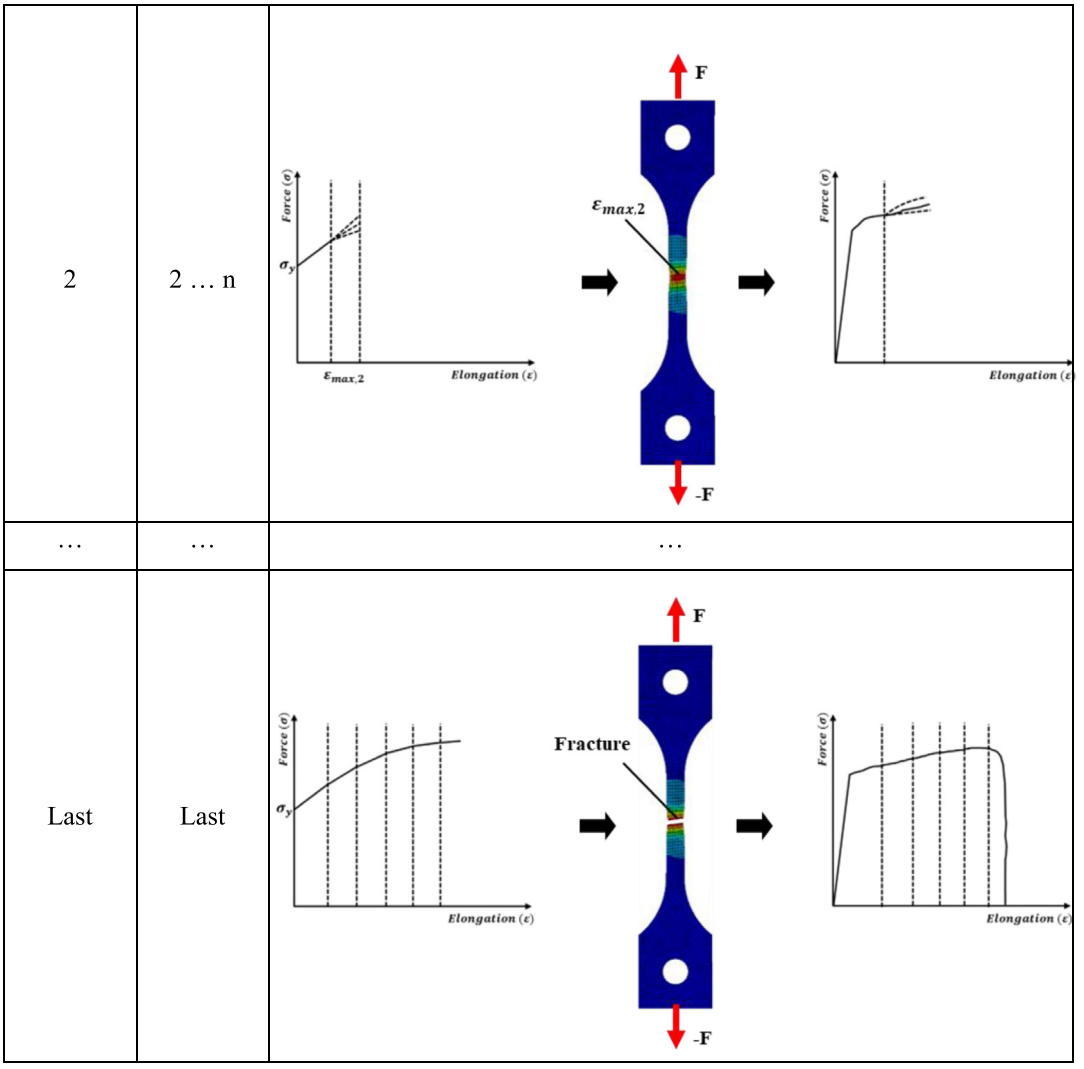

Fig. 6. (*continued*).

$$\%RA = \left(\frac{A_0 - A_f}{A_0}\right) \times 100 \tag{9}$$

where l_f is the fracture length, l_0 is the original gauge length, A_0 is the original cross-sectional area, and A_f is the cross-sectional area at the point of fracture. The %EL depends on the specimen gauge length (l_0) and the %A does not depend on the original cross-sectional area (A_0) and the original gauge length (l_0). However, an alternative method for determining toughness and ductility can be estimated through the characteristics of the engineering stress–strain curve [41], as illustrated in Fig. 8. Then, based on Eq. (8), elongation determines in estimating ductility. The elongation of the engineering stress–strain curve can be measured in the x-axis direction. If the specimen has a greater fracture strain (i.e., total elongation) (from the x-axis means longer) then the material is more ductile, and vice versa. Furthermore, from the engineering stress–strain curve, the absorbed deformation energy up to fracture (i.e., toughness) can be determined from the area under the curve, it can be expressed through Eq. (10).

$$Area = \sigma.\varepsilon = \frac{F}{A}.\frac{\Delta l}{l_0} = \frac{W}{V} = \frac{Energy}{Volume} \tag{10}$$

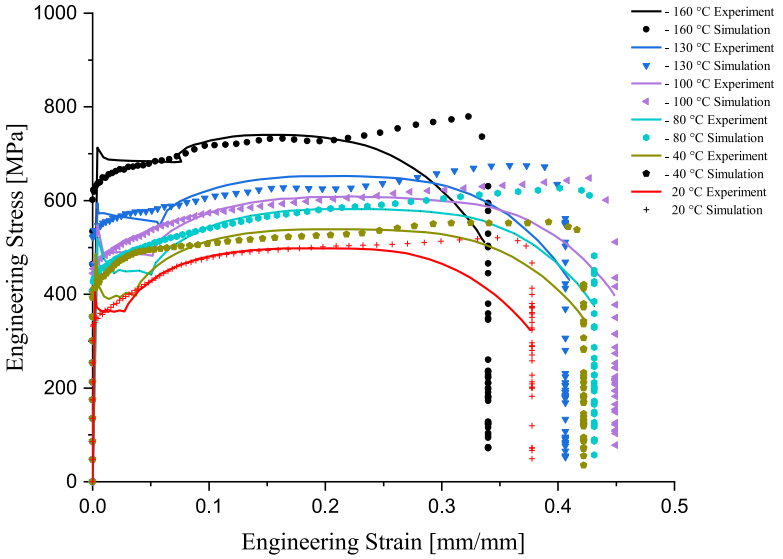

Fig. 7. Comparison of the engineering stress–strain curves from the current simulation and experiment.

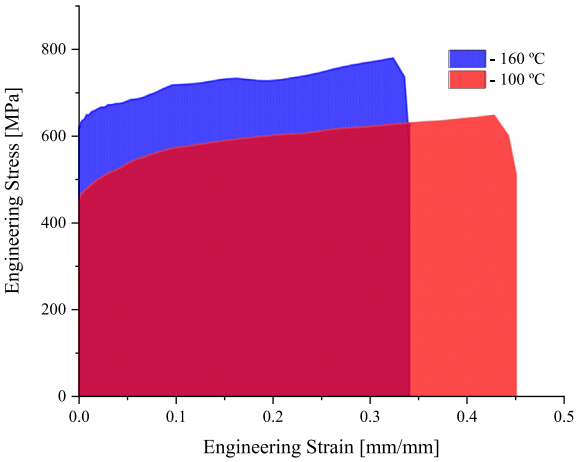

Fig. 8. Comparison of shaded areas indicating mechanical properties (i.e., toughness and ductility)

where σ is the engineering stress, ε is the engineering strain, F is the applied force, A is the cross-sectional area, Δl is the elongation length, and l_0 is the initial gauge length.

It is also indicated that Fig. 8 shows the ratio of the shaded areas at temperatures of −100 °C and −160 °C. Although the ultimate strength of the specimen at −160 °C was higher than the other, the fracture strain was lower than the specimen at −100 °C. The matter indicated that the possible area of the shaded region of the specimen temperature of −160 °C was lower than the specimen temperature of −100 °C. Then, the shaded area at all temperatures was depicted in Fig. 9.

Reduction of temperature affected the degree of ductility and toughness of a material. In Fig. 9, the area of the sample area with temperature 20 °C (room temperature), −40 °C, −80 °C, −100 °C, −130 °C and −160 °C respectively was 182.13, 220.52, 246.37, 267.14, 254.21, and 245.53. The specimen with a temperature 20 °C had the smallest shaded area, while the specimen with a temperature −100 °C had the largest shaded area the biggest. The larger the area of the shaded area, the more challenging the material is, and the longer (in the x-axis direction) the area of the shaded area, the higher the degree of ductility (the more ductile) and vice versa, the more brittle [41].

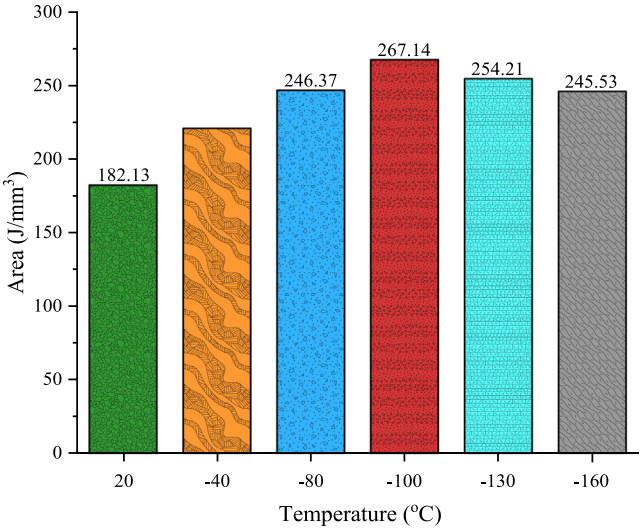

Fig. 9. The area under the engineering stress–strain curve at all temperatures.

In addition, mesh convergence was applied in this study to determine the right mesh size. Different mesh sizes produced results with significant differences. The mesh size used was 1 mm, 2 mm, 4 mm, 6 mm, 8 mm, and 10 mm. Fig. 10a shows that the ultimate strength for room temperature was slightly higher, namely 521.82 MPa, 520.56 MPa, 509.4 MPa, 511.14 MPa, 511.94 MPa, and 546.67 MPa for the mesh size from smallest to largest. Compared to the experimental results, which was 497.07 MPa. The results of the simulation at −40 °C are shown in Fig. 10b. The ultimate strength of the mesh size from most minor to most enormous were 583.12 MPa, 590.74 MPa, 615.67 MPa, 538.09 MPa, 533.23 MPa, and 574.34 MPa. This result was slightly higher than the experimental result, which was 537.81 MPa. The results of the simulation at −80 °C are shown in Fig. 10c. For mesh sizes of 1 mm, 2 mm, 4 mm, 6 mm, 8 mm, and 10 mm, respectively, the ultimate strength was 735.74 MPa, 657.03 MPa, 619.37 MPa, 607.49 MPa, 599.49 MPa, and 645.92 MPa. This result was slightly higher than the experimental result, which was 579.13 MPa. Figs. 10d and 10e show the simulation results at temperatures of −100 °C and −130 °C, respectively. At −100 °C the ultimate strength was obtained at 589.19 MPa, 673.39 MPa, 665.06 MPa, 621.37 MPa, 610.32 MPa, and 603.72 MPa for the mesh size from smallest to largest. For −130 °C, the ultimate strength was 714.4 MPa, 713.25 MPa, 651.28 MPa, 639.81 MPa, 630.76, and 675.82 MPa for the mesh size from smallest to largest. The simulation results were slightly higher than the experimental results, namely 605.10 MPa and 652.28 MPa for temperatures of −100 °C and −130 °C, respectively.

At −160 °C, the ultimate strength obtained from the simulation was 765.42 MPa, 726.52 MPa, 732.48 MPa, 849.22 MPa, 836.65 MPa, and 818.95 MPa for the mesh size from largest to smallest. This result was slightly higher than the experimental result, which was 739.36 MPa, shown in Fig. 10f. Overall, the ultimate strength simulation results agreed relatively well with the experimental results. However, a mesh size that was too large or too small will result in an unfavorable engineering stress–strain curve. Fig. 10 shows that the mesh sizes of 4 mm and 6 mm had the best results, while the mesh sizes of 1 mm and 10 mm had the worst results. On the other hand, the sensitivity of the strain rate in this study was neglected. The rate of application of the load to the specimen or the force applied to the two coupons was constant and did not depend on the reduction of the crossing area in the gauge length area. Based on Eq. (6), because the numerator (force) was constant while the denominator (cross-section area) decreased, the result increased. This is probably the main reason why after the necking phenomenon occurred or reached the maximum stress, the stress value increased, unlike the results of experiments conducted by previous researchers. Nevertheless, the trendline generated in this study had similarities with previous studies. For example, the research conducted by Park et al. [42] who carried out tensile tests at room temperature, Cerik and Choung [43] who examined tensile tests at room temperature and sub-zero, and Zhang et al. [44] who examined the tensile test at room temperature and sub-zero by considering the strain rate.

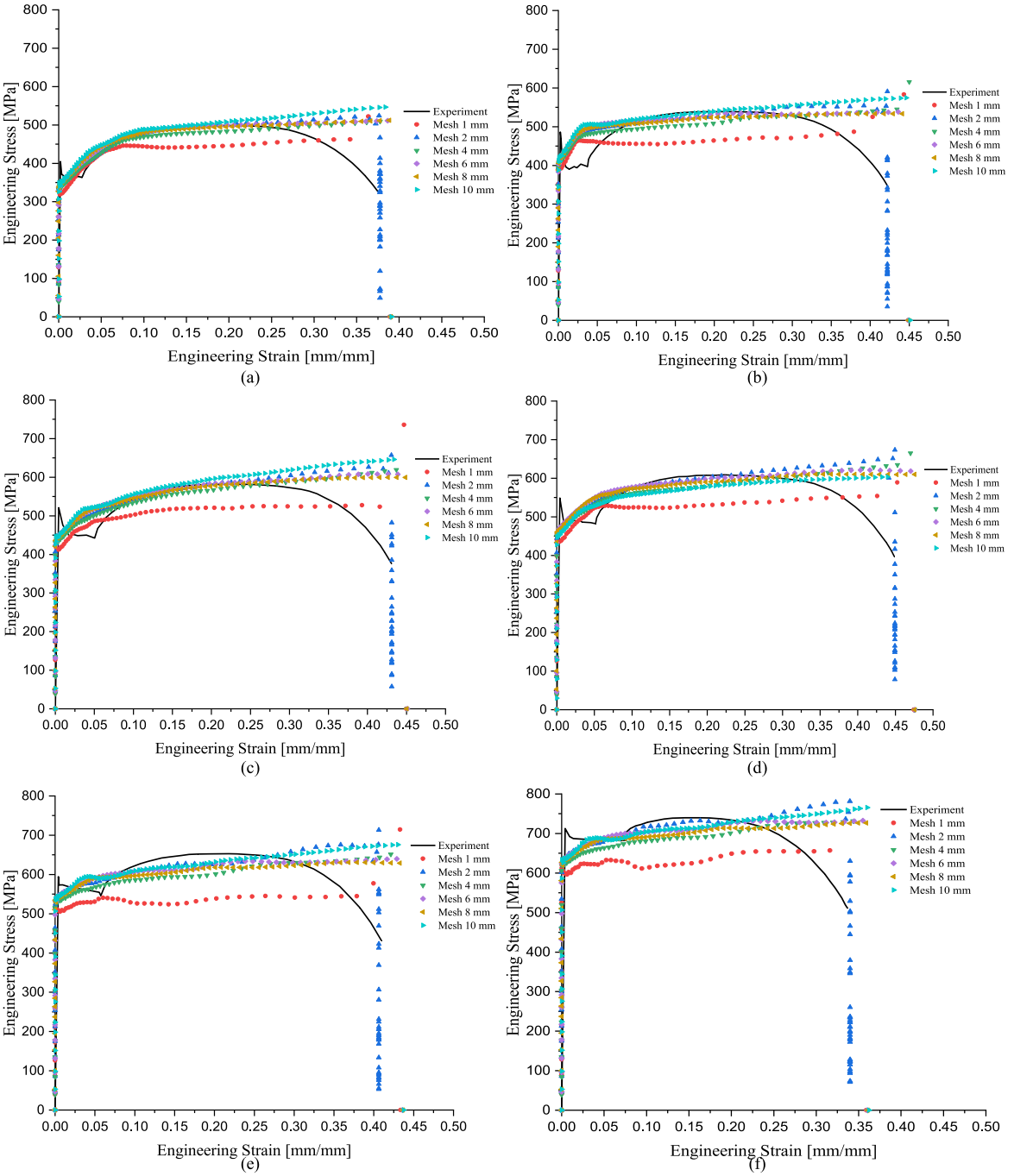

Fig. 10. Comparison of engineering stress–engineering strain curves from current simulation results and experimental results: (a) at 20 °C, (b) at −40 °C, (c) at −80 °C, (d) at −100 °C, (e) at −130 °C, and (f) at −160 °C.

4. Conclusions

Natural gas is the cleanest energy source compared to other energy sources. Therefore, the rate of demand for natural gas is increasing rapidly. Natural gas in its liquefied phase (i.e., LNG) is usually shipped by vessel. NSR (Northern Sea Route) is a maritime route that ships can pass under certain conditions. Because of its location

in the arctic region, harsh weather conditions and extreme temperatures are risks that must be faced. Therefore, research is needed on the response of ship structural materials to extreme temperature conditions to reduce the risk of ship accidents. This study evaluated the response of ship structure materials to low-temperature conditions, such as conditions in the Arctic region, numerically using ANSYS Dynamic Explicit code software.

The resulting engineering stress–strain curve was compared to the stress–strain curve from previous studies. Ultimate strength and fracture strain were used as quantitative parameters to compare the results obtained. Both showed satisfactory results, with an error in ultimate strength $< 10\%$ and an error in fracture strain $< 15\%$. Then, the specimen with a temperature of 20 °C had the lowest toughness because it had the lowest shaded area, and the specimen with a temperature of −100 °C had the highest toughness because it had the largest area. From the point of view of the degree of ductility, the specimen with a temperature of −160 °C was the most brittle because it had the shortest curve length (in the x-axis direction), and the specimen with a temperature of −100 °C was the most ductile because it had the most extended curve length. In addition, different mesh sizes were used to obtain different results. Overall, more mesh sizes were needed to produce better results. Mesh sizes of 4 mm and 6 mm produced the best results in this study.

Further research is required to expand the failure criterion and investigate the sensitivity of the strain rate, which was not investigated in this work. Several failure criteria that may be used include Germanischer Lloyd and Peschmann (based on maximum strain), Rice–Tracey and Cockcroft–Latham (RCTL) (based on maximum stress), etc. Moreover, for the strain rate's sensitivity, it is necessary to do an experimental test to calibrate the parameters in numerical analysis.

Declaration of competing interest

The authors declare that they have no known competing financial interests or personal relationships that could have appeared to influence the work reported in this paper.

Data availability

The authors do not have permission to share data.

References

[1] Mokhatab S, Mak J, Valappil J, Wood D. Handbook of liquefied natural gas 1st edition. Gulf Professional Publishing; 2014.
[2] Jiao Y, Wang Z, Liu J, Li X, Chen R, Chen W. Backtracking and prospect on LNG supply chain safety. J Loss Prev Process Ind 2021;71:104433.
[3] Park J, Lee I, You F, Moon I. Economic process selection of liquefied natural gas regasification: power generation and energy storage applications. Ind Eng Chem Res 2019;58:4946–56.
[4] Dudley B. BP energy outlook. 2017, Available at: https://www.bp.com. [Accessed 22 November 2022].
[5] Kuczyńsk S, Łaciak M, Szurlej A, Włodek T. Impact of liquefied natural gas composition changes on methane number as a fuel quality requirement. Energies 2020;13:5060.
[6] Vallabhuni SK, Lele AD, Patel V, Lucassen A, Moshammer K, Al Abbad M, et al. Autoignition studies of liquefied natural gas (LNG) in a shock tube and a rapid compression machine. Fuel 2018;232:423–30.
[7] Wang T, Zhou Y, Luo Z, Wen H, Zhao J, Su B, et al. Flammability limit behavior of methane with the addition of gaseous fuel at various relative humidities. Process Saf Environ Prot 2020;140:178–89.
[8] Messineo A, Panno G. LNG cold energy in agro-food industry: A case study in Sicily. J Nat Gas Sci Eng 2011;3:356–63.
[9] Łaciak M, Sztekler K, Szurlej A, Włodek T. Possibilities of liquefied natural gas (LNG) use for power generation. IOP Conf Ser Earth Environ Sci 2019;214:012138.
[10] Xu H, Yang D. LNG-fuelled container ship sailing on the Arctic Sea: Economic and emission assessment. Transp Res D 2020;87:102556.
[11] Petroleum B. Statistical review of world energy 71th edition 2021. 2021, Available at: www.bp.com. [Accessed 22 November 2022].
[12] Baek S, Choi W, Kim G, Seo J, Lee S, Jeong H, et al. Liquefied natural gas cold energy utilization for land-based cold water fish aquaculture in South Korea. Energies 2022;15:7322.
[13] Makarova I, Gubacheva L, Makarov D, Buyvol P. Economic and environmental aspects of the development possibilities for the northern sea route. Transp Res Procedia 2021;57:347–55.
[14] Dai L, Jing D, Hu H, Wang Z. An environmental and techno-economic analysis of transporting LNG via Arctic route. Transp Res A 2021;146:56–71.
[15] Theocharis D, Rodrigues VS, Pettit S, Haider J. Feasibility of the northern sea route: The role of distance, fuel prices, ice breaking fees and ship size for the product tanker market. Transp Res 2019;129:111–35.
[16] Østreng W, Eger KM. Shipping in arctic waters: A comparison of the Northeast, Northwest and trans polar passages. Berlin, Heidelberg: Springer; 2013, p. 11–45.

[17] Sarrabezoles A, Lasserre F, Haguoagn'rin Z. Arctic shipping insurance: towards a harmonisation of practices and costs? Polar Rec 2016;52:393–8.
[18] Gleb S, Jin JG. Evaluating the feasibility of combined use of the Northern Sea Route and the Suez Canal Route considering ice parameters. Transp Res A 2021;147:350–69.
[19] Farré AB, Stephenson SR, Chen L, Czub M, Dai Y, Demchev D, et al. Commercial Arctic shipping through the Northeast Passage: routes, resources, governance, technology, and infrastructure. Polar Geogr 2014;37:298–324.
[20] Schøyen H, Bråthen S. The Northern Sea route versus the Suez canal: cases from bulk shipping. J Transp Geogr 2011;19(2011):977–83.
[21] Lasserre F. Case studies of shipping along Arctic routes: analysis and profitability perspectives for the container sector. Transp Res A 2014;66:144–61.
[22] Abbassi R, Khan F, Khakzad N, Veitch B, Ehlers S. Risk analysis of offshore transportation accident in Arctic waters. Int J Marit Eng 2017;159(Part A3):A213–24.
[23] Northern Sea Route Information Office. NSR shipping traffic - transits in 2019. 2020, Available at: https://arctic-lio.com/nsr-shipping-traffic-transits-in-2019/. [Accessed 13 October 2022].
[24] Gunnarsson B. Recent ship traffic and developing shipping trends on the Northern Sea Route-Policy implications for future arctic shipping. Mar Policy 2021;124:104369.
[25] Nam W, Amdahl J. Influence of brittle fracture on the crashworthiness of ship and offshore structures in arctic conditions. In: Conference: The 7th international conference on collision and grounding of ships and offshore structures. Uslan, South Korea: University of Uslan; 2016.
[26] Ehlers S, Ostby E. Increased crashworthiness due to arctic to arctic conditions-The infulence of sub-zero temperature. Mar Struct 2012;28:86–100.
[27] Park DK, Kim DK, Seo JK, Kim BJ, Ha YC, Paik JK. Operability of non-ice class aged ships in the Arctic Ocean-part II. Ocean Eng 2015;102:206–15.
[28] Paik JK, Lee DH, Park DK, Ringsberg JW. Full-scale collapse testing of a steel stiffened plate structure under axial compressive loading at a temperature of −80°C. Ships Offshore Struct 2021;16:255–70.
[29] ISO. Metallic materials tensile testing at low temperature part 3: Method of test at low temperature. Geneva, Switzerland: International Organization for Standardization; 2015, p. 6892–3.
[30] Ridwan R, Nuriana W, Prabowo AR. Energy absorption behaviors of designed metallic square tubes under axial loading: Experiment-based benchmarking and finite element calculation. J Mech Behav Mater 2022;31:443–61.
[31] Prabowo AR, Ridwan R, Muttaqie T. On the resistance to buckling loads of idealized hull structures: FE analysis on designed-stiffened plates. Designs 2022;6:46.
[32] Prabowo AR, Ridwan R, Tuswan T, Imaduddin F. Forecasting the effects of failure criteria in assessing ship structural damage modes. Civ Eng J 2022;8:2053–68.
[33] Cai W, Zhu L, Gudmestad OT, Guo K. Application of rigid-plastic theory method in ship-ice collision. Ocean Eng 2022;253:111237.
[34] Fajri A, Prabowo AR, Muhayat N. Assessment of ship structure under fatigue loading: FE benchmarking and extended performance analysis. Curved Layer Struct 2022;9:163–86.
[35] Prabowo AR, Ridwan R, Muttaqie T. On the resistance to buckling loads of idealized hull structures: FE analysis on designed-stiffened plates. Designs 2022;6:46.
[36] Ren Y, Meng Q, Chen C, Hua X, Zhang Z, Chen Z. Dynamic behavior and damage analysis of a spar-type floating offshore wind turbine under ship collision. Eng Struct 2022;272:114815.
[37] Prabowo AR, Do QT, Cao B, Bae DM. Land and marine-based structures subjected to explosion loading: A review on critical transportation and infrastructure. Procedia Struct Integr 2020;27:77–84.
[38] Ridwan R, Prabowo AR, Muhayat N, Putranto T, Sohn JM. Tensile analysis and assessment of carbon and alloy steels using the FE approach as an idealization of material fractures under collision and grounding. Curved Layer Struct 2020;7:188–98.
[39] Prabowo AR, Ridwan R, Tuswan T, Sohn JM, Surojo E, Imaduddin F. Effect of the selected parameters in idealizing material failures under tensile loads: Benchmarks for damage analysis on thin-walled structures. Curved Layer Struct 2022;9:258–85.
[40] Dowling NE. Mechanical behavior of materials: engineering methods for deformation, fracture, and fatigue 4th edition. London, United Kingdom: Pearson Education; 2012.
[41] Callister WD, Rethwish DG. Materials science and engineering an introduction 9th edition. United States of America: Wiley Publisher; 2013.
[42] Park SJ, Cerik BC, Choung J. Comparative study on ductile fracture prediction of high-tensile strength marine structural steels. Ships Offshore Struct 2020;15:S208–19.
[43] Cerik BC, Choung J. On the prediction of ductile fracture in ship structures with shell elements at low temperatures. Thin-Walled Struct 2020;151:106721.
[44] Zhang J, Kang X, Shi X, Soares CG, Song M. Low temperature effect on the mechanical properties of EH36 with strain rates. J Mar Sci Eng 2023;11:678.